Materials Today Chemistry 30 (2023) 101514

Contents lists available at ScienceDirect

Materials Today Chemistry

journal homepage: www.journals.elsevier.com/materials-today-chemistry/

Long-lived NIR emission in sulfur-doped zeolites due to the presence of $[S_3]^{2-}$ clusters

Catarina Viola [a, b], César A.T. Laia [a], Mani Outis [a], Luís F.V. Ferreira [c], Luís C. Alves [d], Miguel Teixeira [e], Filipe Folgosa [e], João C. Lima [a], Andreia Ruivo [b, **], João Avó [c, *]

[a] LAQV-REQUIMTE, Department of Chemistry, NOVA School of Science and Technology, FCT NOVA, Universidade NOVA de Lisboa, 2829-516 Caparica, Portugal
[b] VICARTE, Vidro e Cerâmica para As Artes, NOVA School of Science and Technology, FCT NOVA, Universidade NOVA de Lisboa, 2829-516 Caparica, Portugal
[c] BSIRG-iBB-Institute for Bioengineering and Biosciences and Associate Laboratory I4HB—Institute for Health and Bioeconomy at Instituto Superior Técnico, Universidade de Lisboa, 1049-001 Lisboa, Portugal
[d] C2TN (Campus Tecnológico e Nuclear, IST/UL), Estrada Nacional 10 2695-066 Bobadela, Portugal
[e] Instituto de Tecnologia Química e Biológica António Xavier, Universidade Nova de Lisboa, Av. da República, 2781-901 Oeiras, Portugal

ARTICLE INFO

Article history:
Received 17 January 2023
Received in revised form
16 March 2023
Accepted 18 March 2023
Available online 19 April 2023

Key words:
Luminescent materials
Chalcogen-doped zeolites
Near-infrared luminescence
Optical spectroscopy
Time-resolved spectroscopy

ABSTRACT

The exploration of novel long-lived near-infrared (NIR) luminescent materials has attracted significant attention due to their applications in optical communications, anticounterfeiting, and bioimaging. However, these materials usually present low photoluminescence quantum yields and low photo- and chemical stability. Novel emitters that overcome these limitations are in demand. In this study, NIR emission was achieved using widely available, sustainable, and non-toxic materials through the synthesis of sulfur-doped zeolites, with different S/Cl ratios. With a combination of computational calculations (TD-DFT) and spectroscopic data, this emission was assigned to the radiative decay of excited triplet states of $[S_3]^{2-}$ clusters, which resulted in a remarkably high Stokes shift (1.97 eV, 440 nm) and an average decay time of 0.54 ms. These new materials present high stability, external quantum efficiency of up to 17%, and a long-lived NIR emission, placing these compounds in a unique position to be used in applications demanding NIR emitters.

1. Introduction

Over the last decade, the interest in near-infrared (NIR)-emitting molecules and materials has constantly increased, mainly due to their potential in applications such as *in vivo* imaging, anticounterfeiting tags, and optical communications. The importance of these materials in biological systems arises mainly because light scattering in this region is much reduced, allowing deep tissue penetration, and autofluorescence phenomena are insignificant [1–3]. In anticounterfeiting and authentication, NIR-emitting optical tags [4,5] enable covert security elements with both probe excitation and emission in spectral regions that lack detection by the human eye, requiring instrumental verification and increasing security level. Another high-demand field for NIR emitters is in optical communications, where they are generally believed to increase material stability and device durability [6] and to allow reaching longer communication distances and higher bandwidths [7,8]. NIR emitters can also be explored as phosphors in lighting devices through NIR phosphor-convert light-emitting diodes (NIR pc-LEDs), in which the coating of a blue LED with a broadband NIR emitter produces compact, highly efficient and low cost devices [[9]]. This enables overcoming the narrow emission bands found in NIR-LED, which limits their applicability [10].

A drawback of working with NIR emitters is that, generally, they possess low photoluminescence quantum yields (PLQYs) that result from the increase of non-radiative pathways (energy gap law) [2,11]. In addition, most materials with NIR emission are poorly available and/or lack chemical- and photostability [12,13].

In this sense, zeolites can provide a sustainable alternative for many of these drawbacks, as they are low cost materials that can host and stabilize NIR emitting molecules [14,15], promoting a significant increase in their luminescence quantum yields [16,17].

* Corresponding author.
** Corresponding author.
E-mail addresses: a.ruivo@fct.unl.pt (A. Ruivo), joao.avo@tecnico.ulisboa.pt (J. Avó).

https://doi.org/10.1016/j.mtchem.2023.101514

Rare-earth elements and bismuth have been used as dopants in sodium aluminosilicate zeolites that exhibit NIR emission [18–21]. But tellurium and sulfur dopants can also confer NIR photoluminescence to these materials. Sulfur is particularly significant as a luminescent dopant since it is an abundant and non-toxic element, allowing for inexpensive synthesis with low environmental impact [22], contrary to rare-earth and heavy-metal elements, which are present in the European Union list of critical raw materials in, according to the European Commission (2020) [23]. Sulfur-doped zeolites (previously known as hackmanites) are an example of natural aluminosilicate minerals, with well-known optical properties that include tenebrescence (photochromism) and luminescence across the visible spectrum, depending on the sulfur species present [24]. In 1954, Kirk published the first report on the synthesis and characterization of luminescent sulfur-doped aluminosilicates zeolites (sodalites) with emissions varying from visible to NIR region (maximum >700 nm) [25]. Since then, the emission in the visible region (yellow-orange) of sodalite has been extensively studied and was ultimately assigned to the presence of $[S_2]^-$ clusters. The involved states are $[2]\Pi_g$ and $[2]\Pi_u$, resulting in an absorption at *ca.* 390 nm and a characteristic emission spectrum centered at around 650 nm, with vibronic peaks separated by *ca.* 560 cm^{-1} (20–25 nm) [26,27]. $[S_2]^-$ exhibits external quantum efficiencies (EQEs) up to 53% and a high temperature stability of up to 450 °C [21]. The NIR emission, however, was only investigated later in 2009 by Gaft and coworkers who reported a long-lived NIR emission spectrum in a sodalite mineral of natural origin with a decay time of 3.6 ms [24]. In addition, our group recently tackled the synthesis of NIR-emitting zeolites, varying their chalcogen proportion in a systematic study [21]. However, we have identified a lack of consistent information regarding the properties and origins of the NIR emission. Herein, we focus on the photophysical aspects of these NIR emissive materials and report a detailed spectroscopic and computational analysis to understand and finally propose a mechanism for this phenomenon and open the path to synthesize a new class of NIR emitters based on chalcogen-doped zeolites.

2. Experimental

2.1. Synthesis and structural characterization

The sulfur-doped zeolite samples were prepared following equation (1), according to the stoichiometry $Na_8Si_6Al_6O_{24}S_xCl_{2-2x}$, via solid-state synthesis.

$$3\,Na_2Si_2Al_2O_8 + x\,Na_2SO_3 + (2-2x)NaCl \rightarrow Na_8Si_6Al_6O_{24}S_xCl_{2-2x} + \frac{3}{2}xO_2 \quad (1)$$

Appropriate amounts of NaCl (Honeywell), Na_2SO_3 (Honeywell), and Na-LTA zeolite (Honeywell) were mixed, considering the desired stoichiometry, with x = 0, 0.1, 0.2, 0.3, 0.4, 0.5, 0.6, 0.7, 0.8, and 0.9. Zeolite Na-LTA was first dried at 500 °C for 5 h. Afterward, these powder mixtures were ball-milled for 1 h and homogenized in a shaker powder mixer for 3 h. The nominal molar ratios of S/Cl, correspond to 0, 0.06, 0.13, 0.21, 0.33, 0.50, 0.75, 1.17, 2.0, and 4.5, respectively.

The synthesis was performed in an electric furnace (TH1300, Termolab) at 900 °C for 1 h, under a reducing atmosphere of 5% H_2, 95% Ar (v/v) at 500 mL/min. These materials were washed with water and ethanol to remove any trace of reagents.

A sample of commercial Na-LTA zeolite without any pretreatment was submitted to the same synthesis procedure.

2.1.1. X-ray powder diffraction

A X-ray diffractometer (XRD) Rigaku model MiniFlex II with Cu X-ray tube (30 KV/15 mA) was used over a 2θ range of 10°–70° with a scan speed of 1°/min.

2.1.2. Particle-induced X-ray emission (PIXE)

The powdered samples were compressed into pellets and analyzed with a 700 keV proton beam generated by the 2.5 MV Van de Graaff accelerator installed at CTN/IST through PIXE technique. An 8 μm Be-windowed silicon drift detector (SDD) detector was used for the acquisition of the produced X-rays, while GupixWin software accounted for the spectra deconvolution and quantitative analysis. The major sample constituent elements (for Na and heavier elements) were taken in their oxide form and composition normalized to 100%. The results are presented in Table 1 and Supplementary Table 2 represents the average and standard deviation obtained with the analysis of three different pellets for each sample type. The validation of experimental conditions and procedures was determined through the analysis of Corning B glass reference material.

2.2. Optical characterization

2.2.1. Diffuse reflectance

Diffuse reflectance measurements were performed inside an integrating sphere in a Shimadzu UV-2501PC using $BaSO_4$ as a reference sample.

The ultramarine blue pigment (ultramarine blue DP-55 from Nubiola) was diluted with $BaSO_4$ until it matched the same absorbance at 600 nm found in the sample S/Cl = 4.5. This diluted sample was used as a reference for $[S_3]^-$ species in Raman and EPR spectroscopies.

2.2.2. Electron paramagnetic resonance (EPR) spectroscopy

X-band EPR spectra were obtained at 120 K using a Bruker EMX spectrometer equipped with a liquid nitrogen continuous flow cryostat, and a high sensitivity perpendicular mode rectangular cavity. Powder samples were packed into quartz EPR tubes (3 mm I.D.). All spectra were recorded using a microwave frequency of 9.45 GHz, a modulation amplitude of 0.1 mT and a microwave power of 2 mW. Spectra were analyzed and simulated using SpinCount [54].

2.2.3. Micro-Raman microscopy

Raman microspectroscopy was carried out using a Labram 300 Jobin Yvon spectrometer equipped with a HeNe laser. Each spectrum was collected using 632.8 nm excitation and a 50× objective.

2.2.4. Steady-state luminescence

The excitation (λ_{em} = 725 nm) and emission (λ_{exc} = 355 nm) spectra were recorded using a Horiba Jobin Yvon fluorolog FL3-22 fluorimeter equipped with a xenon 450 W light source.

Table 1
Molar percentage of each main element found in zeolite samples using particle-induced X-ray emission (PIXE) technique.

Nominal S/Cl	Molar percentage composition (%)[a]						Obtained S/Cl
	Na	Si	Al	O	S	Cl	
0	15.69	13.37	13.01	54.33	0.00	3.26	0
0.21	15.75	13.39	13.01	54.77	0.12	2.62	0.05
4.5	15.55	13.66	13.15	56.54	0.50	0.27	1.82

[a] Calculated from the PIXE weight percentage (wt%) (Supplementary Table 2).

The EQEs of the powder samples were measured by the absolute method using an integrating sphere. A National Institute of Standards Technology (NIST) calibration lamp was used to compute the correction curve of the integrating sphere/detection system. The excitation source used was a 355 nm continuous laser (Laser-Technic, 10 mW). The signals were collected from the integrating sphere by a collimating beam probe coupled to an optical fiber (fused silica) in this way, assuring the connection to the monochromator entrance. A fixed monochromator (Andor, Shamrock 163) coupled to an ICCD detector (Andor, i-Star 720) with time gate capabilities was used in the accumulation mode [55].

2.3. NIR emission characterization

The luminescence decays were measured by the single-photon timing method using a Horiba DeltaFlex system with a BH 402.9 nm laser excitation, operating in burst mode for 50 MHz. Emission wavelengths were selected with a monochromator with 3 or 6 nm bandwidth (selected according to the emission intensity of each sample), centered at 800 nm, and detected with a pixelated photon detector (PPD) detection module.

In the time-resolved emission spectroscopy study, two different detectors were used. One more sensitive in the UV—Vis range and the other more accurate in the NIR region, according to [56].

The phosphorescence emission spectra of all sulfur-doped zeolite samples were carried out in a UV—Vis detector Jobin Yvon FluoroLog fluorescence spectrometer with a pulsed xenon lamp with full width at half-maximum of 3 μs was used. A delay time of 0.1 ms (Supplementary Fig. 3) was applied. In addition, room temperature lifetime measurements of all synthesized powders were carried out in the same UV—Vis detector.

For more accurate results in the NIR region a NIR-sensitive detector ICCD (with a minimum temporal gate of 2.2 ns) was used. Here, a further study of sample 4.5 was performed using as an excitation pulsed a N_2 laser at 337 nm (OBB, model 4500 with ~1 mJ per pulse). A fixed monochromator (Andor, Shemrock 163) coupled to an ICCD detector (Andor, i-Star 720) with time gate capabilities and in the kinetics mode was used here to detect the fluorescence or phosphorescence signals. The signals were collected by a collimating beam probe coupled to an optical fiber (fused silica) in this way, assuring the connection to the monochromator entrance. The time-resolved emission spectroscopy (TRES) spectra of the sample S/Cl = 4.5 have been acquired in a short-time or long-time domains using suitable gate widths (1μs and 1 ms) and start delays (see Fig. 4A e 4. B).

2.3.1. Transient absorption (TA) spectroscopy

Laser flash photolysis experiments were carried out with the fourth harmonic of a Nd:YAG laser (266 nm, ca. 6 ns FWHM, 35 mJ/pulse) in the diffuse reflectance mode. The light arising from the irradiation of solid samples by the laser pulse and monitoring lamp (Xe 450 W) was collected by a collimating beam probe coupled to an optical fiber (fused silica) and was detected by a gated intensified charge coupled device Oriel model Instaspec V (Andor ICCD, based on the Hamamatsu S57 69—0907). The intensified charge-coupled device (ICCD) was coupled to a fixed imaging compact spectrograph (Oriel, model FICS 77441). The system can be used either by capturing all light emitted by the sample or in a time-resolved mode by using a delay box (Stanford Research Systems, model D6535). The ICCD has high-speed gating electronics (2.2 ns) and intensifier and covers the 200—950 nm wavelength range. Time-resolved absorption spectra of the powdered sample have been acquired in a short-time or long-time domains using a fixed gate width of 2 μs and suitable start delays. For a small percentage of conversion (high concentration of ground state absorbers and low-laser fluencies), the concentration of transients decreases exponentially and transient absorption data were reported as percentage of absorption (% Abs.), defined by equation 2:

$$\%\,Abs = 100\,\frac{\Delta J_t}{J_0} = \left(1 - \frac{J_t}{J_0}\right)100 \qquad (2)$$

where J_o and J_t are diffuse reflected light from sample before exposure to the exciting laser pulse and at time t after excitation, respectively, see Fig. 4D [57].

2.4. Computational studies

DFT calculations have been carried out with the program Gaussian 16 using the B3LYP functional and Def2TZVP triple zeta basis set for S. All calculations, that is, geometry optimization and TD-DFT were performed in gas phase. For molecular orbital visualization, Avogadro 1.2.0 was employed.

3. Results and discussion

3.1. Synthesis and structural characterization

The luminescent sulfur-doped aluminosilicates zeolites were synthesized by mixing Na-LTA zeolite, NaCl, and Na_2SO_3, followed by a heat treatment at 900 °C for 1 h, under a reducing atmosphere following the stoichiometry $Na_8Si_6Al_6O_{24}S_xCl_{2-2x}$. Samples with nominal molar ratios of S/Cl = 0, 0.06, 0.13, 0.21, 0.33, 0.50, 0.75, 1.17, 2.0, and 4.5 were produced.

The samples were analyzed through X-ray powder diffraction (XRPD) (Fig. 1B and Supplementary Fig. 1). The crystalline phase of Na-LTA was not detected in the XRPD data. However, three different crystalline phases were found, sodalite, nepheline, and carnegieite (see Fig. 1A), which are known to form at high temperatures from zeolite Na-LTA [28,29]. Contrary to the two polymorphs (nepheline and carnegieite) that only need a high temperature to be formed, sodalite also requires the presence of NaCl. Presumably, the sodalite cages (common building units present in both Na-LTA and sodalite phases) are preserved due to chloride anion incorporation and consequent stabilization. Sodium also plays a crucial role to ensure the charge balance in the structure [30]. The relative fractions of these three crystalline phases are summarized in Fig. 1C and in Supplementary Table 1, with the sodalite phase decreasing and both nepheline and carnegieite increasing with the S/Cl ratio. Sodalite phase behavior can be explain by the decreasing of NaCl amount during the synthesis with the increase of S/Cl ratio. Therefore, nepheline and carnegieite formation will be favored.

To determine the elemental composition of the produced materials, the elemental analysis was conducted through PIXE technique (Supplementary Table 2). Table 1 summarizes the concentration of the most relevant elements found in molar percentage for S/Cl = 0, 0.21, and 4.5 samples, which are representative of different sulfur concentrations.

These results show that the Si/Al ratio from the initial Na-LTA is not affected by our synthesis and doping process, remaining *ca.* 1 in all samples [35]. The samples also contain small traces of potassium, calcium, titanium, and iron impurities that were present in the starting materials. Furthermore, it is evidenced that the sulfur-doping process was successful, as the S/Cl ratio increases with increasing sulfite amount during synthesis.

3.2. Optical characterization

The optical properties of the prepared sodium aluminosilicate zeolite samples were characterized by diffuse reflectance and

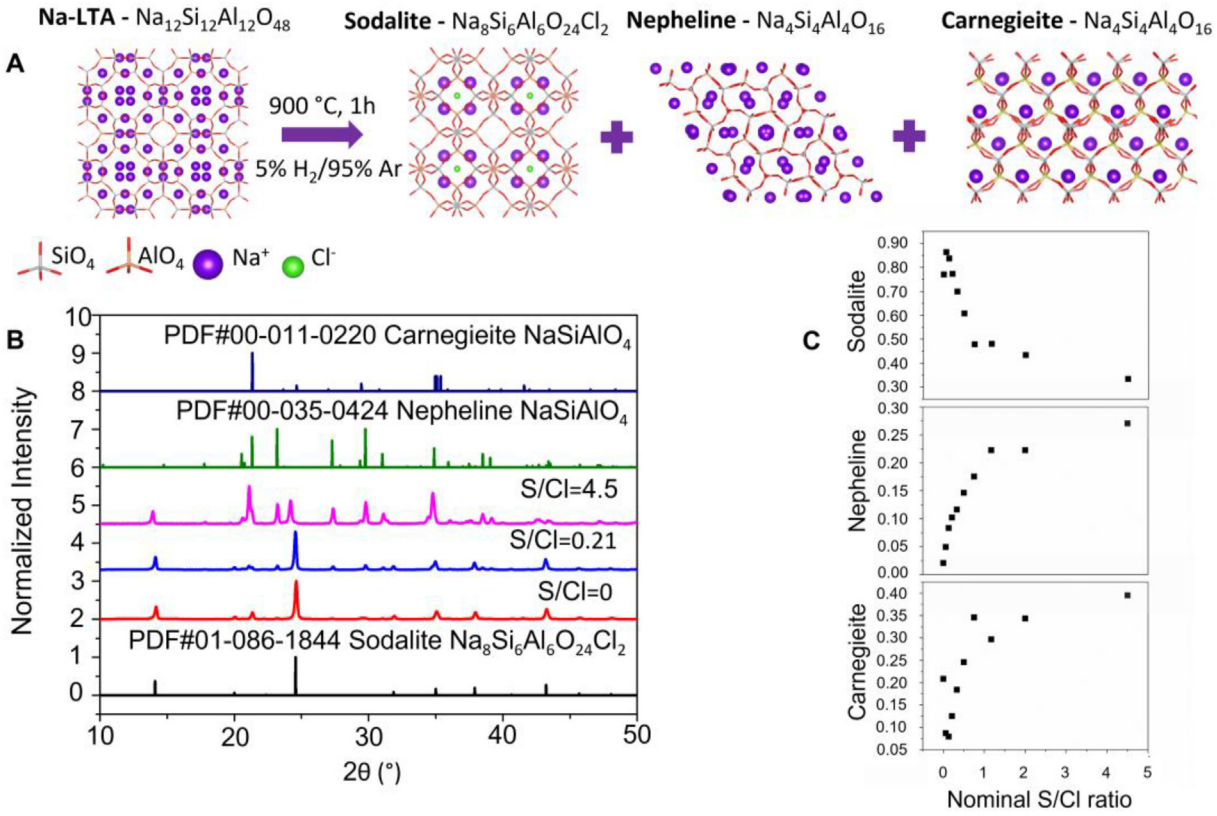

Fig. 1. – Structural analysis of sulfur-doped zeolite samples. (A) Proposed synthesis scheme, adopted from crystallographic data [31–34]. (B) X-ray powder diffraction patterns of the synthetized sulfur-doped zeolite samples with different S/Cl ratios and the ICDD standard card of 01-086-1844 sodalite ($Na_8Si_6Al_6O_{24}Cl_2$), 00-035-0424 nepheline ($NaSiAlO_4$), and 00-011-0220 carnegieite ($NaSiAlO_4$). (C) Sodalite, nepheline and carnegieite fractions calculated in the synthesized zeolite samples.

luminescence spectroscopy. Fig. 2A depicts the diffuse reflectance spectra for the prepared zeolite samples after transformation using the Kubelka-Munk theory [36]. At low concentrations (S/Cl < 0.33), the spectra are dominated by a band centered at 390 nm. This absorption band is in good agreement with the $[2]\Pi_g \rightarrow [2]\Pi_u$ transition described for $[S_2]^-$ clusters [37]. The 390 nm band disappears at higher sulfur content, and two new absorption bands appear at *ca.* 355 and 600 nm. The latter band is assigned to $[S_3]^-$ clusters in sodalite, well-known for their absorption at around 600 nm [37], which are found in several minerals [38] and are commonly known as the ultramarine blue pigment. The presence of both $[S_2]^-$ and $[S_3]^-$ species was confirmed by Raman and EPR spectroscopies (Fig. 2.E and 2.F, respectively) [38–41]. However, the species responsible for the absorption at 355 nm was not previously identified. Excitation with UV-light leads to emission spectra depicted in Fig. 2B. In samples with low-sulfur content (S/Cl < 0.33), the characteristic band with a vibronic resolution of $[S_2]^-$ centered at around 635 nm was detected, increasing in intensity with sulfur concentration [42,26]. At high-sulfur content (S/Cl > 0.5), a new emission band centered at 725 nm, lacking vibronic resolution, starts to be observed, becoming dominant at S/Cl = 4.5. The excitation spectra of these samples reveal that these emission bands arise from different species (Fig. 2C). The band at 635 nm corresponds to the species absorbing at 390 nm, $[S_2]^-$, while the NIR-emitting species is responsible for the absorption at 355 nm. The excitation spectrum of the sample S/Cl = 4.5, detected at 725 nm, shows only the band at 355 nm (Fig. 2D), overlapping the K-M spectrum.

These results seem to indicate that sulfur is responsible for the differences found in both K-M and emission spectra, in opposition to the previous assignment of Fe^{3+} impurities [24]. Indeed, according to our PIXE results, the iron concentration detected in the sulfur-doped samples was the same (Supplementary Table 2), not explaining the variation in the optical properties. The same NIR emission was also found in zeolite Na-LTA samples submitted to the same experimental procedure (temperature and atmosphere) as the sulfur-doped samples (Fig. 3A) and can be assigned to the presence of small traces of sulfur in the zeolite Na-LTA (Supplementary Table 2). Furthermore, the XRPD data indicated that these sample are composed only by nepheline and carnegieite crystalline phases, without any sodalite (Fig. 3B). Suggesting that the NIR emission does not arise from any sulfur species in sodalite, contrary to initial predictions, and that it should occur from nepheline and/or carnegieite phases. The lack of sodalite phase can be explained by the absence of NaCl during the synthesis.

The Raman band at 550 cm^{-1} is attributed to the vibrational modes ν_1 of $[S_3]^-$ clusters [41,39] (Fig. 2E). Besides, from 400 to 500 cm^{-1} are the framework vibrations of sodalite, nepheline, and carnegieite [43–45]. Additionally, the EPR spectra of the samples S/Cl = 0, 0.21, and 4.5 and commercial ultramarine blue pigment (UBP) were recorded at 120 K and are present in Fig. 2F. These spectra were deconvoluted in order to obtain the present species (see Supplementary Fig. 2), the obtained results are summarized in Table 2. Sample S/Cl = 0.21 shows two rhombic signals correspondent to two different species, $[S_2]^-$ and $[SO_2]^-$, with identical contributions, and were simulated with g-values of 2.002, 2.012, and 2.032 and 2.002, 2.008, and 2.019, respectively. The assignment of $[S_2]^-$ was supported by both the absorption and emission spectroscopy characterizations, which undoubtedly confirm its presence in sample S/Cl = 0.21. It should be noted that the parameters

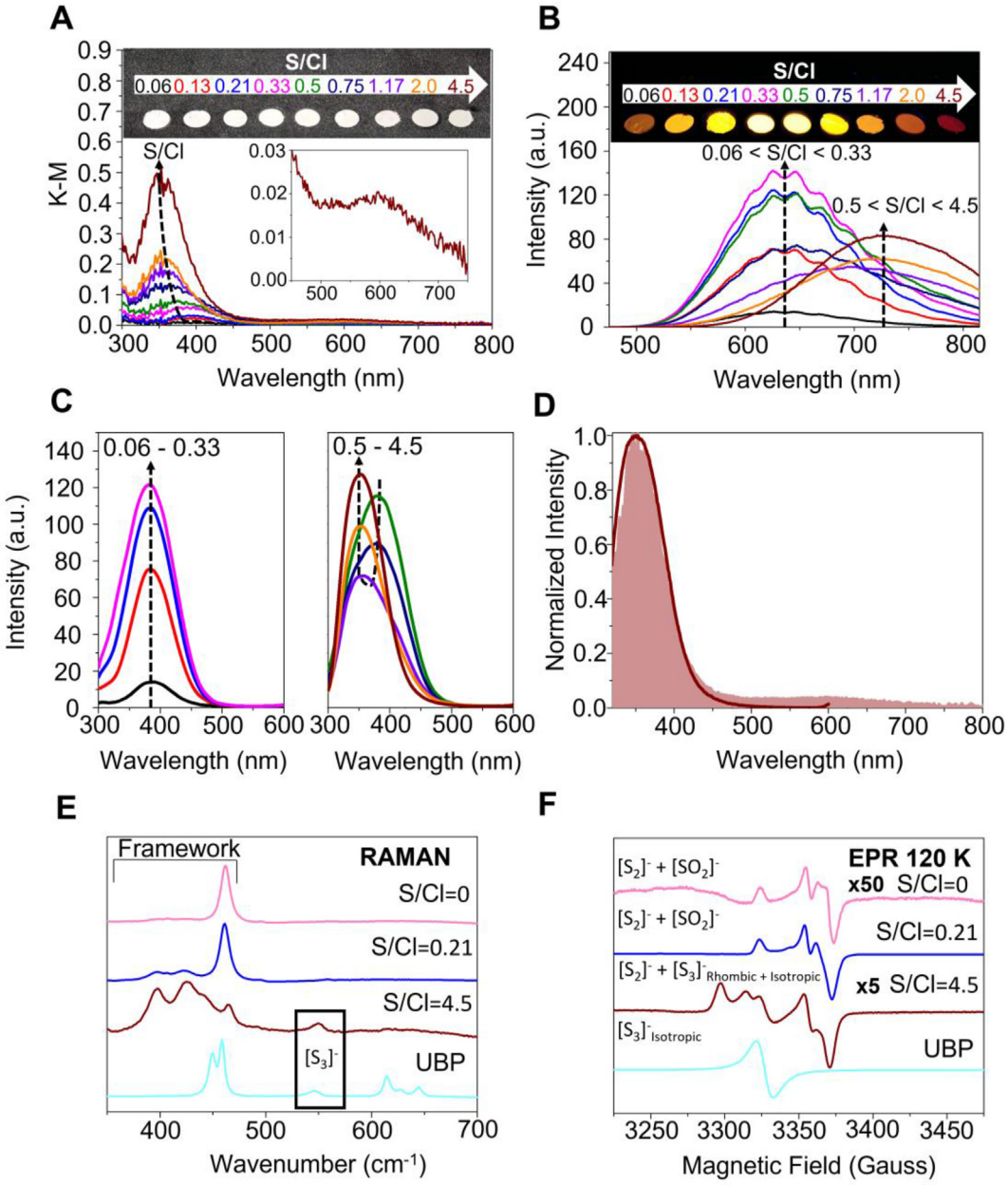

Fig. 2. – Steady-state material optical characterization. (A) Diffuse reflectance spectrum of samples with different sulfur content. The inset on top depicts photos of the samples under ambient light. The inset on the right shows a close-up of the sample S/Cl = 4.5 in the 450–750 nm region. (B) Steady-state emission spectra of samples with different sulfur content (λ_{exc} = 355 nm). The inset on top depicts photos of the samples under UV light (λ_{exc} = 365 nm). (C) Excitation spectra of synthetized samples (left) 0.06 < S/Cl < 0.33 and (right) 0.5 < S/Cl < 4.5 (λ_{em} = 725 nm). (D) Overlap of Kubelka-Munk (light-brown) with excitation (dark-brown) spectra of sample S/Cl = 4.5. (E) Raman and (F) electron paramagnetic resonance (EPR) spectra of the samples S/Cl = 0, 0.21, and 4.5 and commercial ultramarine blue pigment (UBP), used as reference for $[S_3]^-$ cluster. Note the multiplication factor applied in the EPR spectrum of S/Cl = 0 and 4.5. For EPR spectra deconvolution, see Supplementary Fig. 2.

found in the literature for this radical anion are very divergent [38,39,46]. On the other hand, the g values obtained for $[SO_2]^-$ are compatible with that previously described by Schneider and co-workers in KCl crystals doped with sulfur [47]. The presence of this species in this sample is, presumably, related to the synthesis process where the $[SO_3]^{2-}$ was not totally reduced to $[S_2]^-$. The latter species is also present in the samples S/Cl = 0 and 4.5, with essentially the same g-values. In fact, the blank sample presents the same two species, $[S_2]^-$ and $[SO_2]^-$, identified in the sample S/Cl = 0.21 but with slight differences regarding their individual contribution to the spectrum, 50/50%. On the contrary, in the sample S/Cl = 4.5, besides the contribution of species $[S_2]^-$ with 40%, two other species are identified, accounting for 35% and 25%, respectively. The first one was simulated with g values of 2.003, 2.034, and 2.048, which are in accordance with the presence of an $[S_3]^-$ species, similarly to that previously [39,40]. These data are also in agreement with the results obtained by absorption and Raman spectroscopies (Fig. 1.A and 1.E). The second species, contrary to the previously described species, has an isotropic signal with g = 2.029, correspondent to $[S_3]^-$. This is similar to the described by Chukanov and coworkers [38], where $[S_3]^-$ is in a homogeneous environment in the sodalite cages. This species was also observed in the

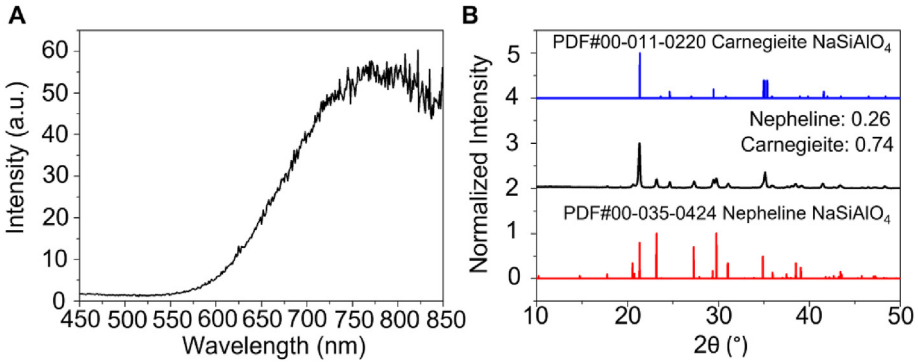

Fig. 3. – Characterization of zeolite Na-LTA sample after 1h at 900 °C, under reductive atmosphere. (A) Emission spectra (λ_{exc} = 355 nm). (B) X-ray powder diffraction diffractogram and relative crystalline phases and comparison with the ICDD standard card of 00-035-0424 nepheline ($NaSiAlO_4$) and 00-011-0220 carnegieite ($NaSiAlO_4$).

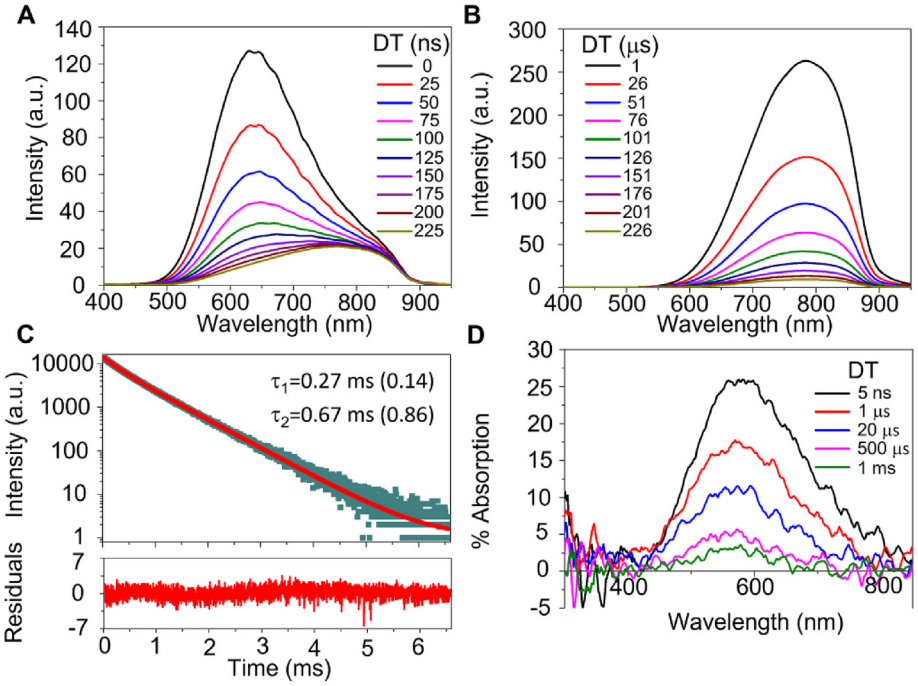

Fig. 4. - Time-resolved spectroscopies of sample S/Cl = 4.5. (A and B) Emission spectra at different delay times, DT, (λ_{exc} = 337 nm). (C) (Above) Photoluminescence decay (dotted line) and respective bi-exponential fitting (solid line) at 800 nm (λ_{exc} = 402.9 nm) and (Below) corresponding residuals. (D) Transient absorption spectra at different delay times (λ_{exc} = 266 nm).

Table 2
g-values, relative percentages, and species assignment present in the samples S/Cl = 0, 0.21, and 4.5 and commercial ultramarine blue pigment (UBP).

Sample S/Cl	Species assignment	g_1	g_2	g_3	Relative contribution (%)
0	$[S_2]^-$	2.000	2.013	2.031	50
	$[SO_2]^-$	2.000	2.005	2.012	50
0.21	$[S_2]^-$	2.002	2.012	2.032	40
	$[SO_2]^-$	2.002	2.008	2.019	60
4.5	$[S_2]^-$	2.002	2.012	2.031	40
	$[S_3]^-$ rhombic	2.003	2.034	2.048	35
	$[S_3]^-$ isotropic	2.029	2.029	2.029	25
UBP	$[S_3]^-$ isotropic	2.029	2.029	2.029	100

spectrum obtained for the commercial ultramarine blue pigment (UBP), used as a reference for $[S_3]^-$, that contains this radical species. Therefore, both species can be attributed to the presence of $[S_3]^-$ radical but in different local environments.

In summary, EPR spectroscopy shows that the increase in the sulfur concentration leads to *ca.* 5-fold reduction in the intensity of the EPR signals (see multiplication factors in Fig. 2F), indicating a smaller concentration of paramagnetic species in the sample S/Cl = 4.5 than in sample S/Cl = 0.21. This corroborates the absorption and emission data collected from sample S/Cl = 4.5, which suggests the presence of both $[S_2]^-$ and $[S_3]^-$ (paramagnetic) in low concentrations and indicates that a non-paramagnetic species is responsible for the absorption band at *ca.* 355 nm and the NIR emission.

In addition to this characterization, since sulfur-doped sodalite materials are well known for their photochromic properties due to the presence of S_2^{2-} species, this behavior was also assessed [24]. Thus, the prepared powder samples were irradiated at 254 nm to analyze whether the typical induced pink color would appear. However, no color change was detected after irradiation, suggesting that the S_2^{2-} species are absent or in negligible concentration in the prepared materials.

3.3. NIR emission characterization

The decay times of all the samples were measured at λ_{em} = 800 nm. They fit well with the following bi-exponential equation (3), see Fig. 4C.

$$y = A_1 \times e^{\frac{-x}{\tau_1}} + A_2 \times e^{\frac{-x}{\tau_2}} + y_0 \quad (3)$$

An average decay time of 0.54 ± 0.027 ms was obtained for all samples at room temperature (Supplementary Table 3). The intensity of this long-lived emission increased with the S/Cl ratios, see Supplementary Fig. 3, suggesting that the emission arises from a spin-forbidden transition of a sulfur species. The same bi-exponential decay was found in the sample composed only by nepheline and carnegieite crystalline phases (Supplementary Fig. 4), further confirming that the NIR emission is not associated with sodalite cages.

The time evolution of the emission characteristics of sample S/Cl = 4.5 was studied in more detail by acquiring the spectra at different time delays (Fig. 4.A and 4.B) after excitation. At shorter times $[S_2]^-$ characteristic emission is registered, while the NIR emission dominates at longer times. These results indicate that a fraction of $[S_2]^-$ is still present in the samples even at the higher sulfur concentration, mainly due to the existence of sodalite crystalline phase in this sample. Through transient diffuse reflectance spectroscopy, we also observed the transient absorption of a long-lived species centered at *ca.* 580 nm. This can be attributed to a triplet-triplet absorption band, further supporting the hypothesis that the long-lived emission is due to the presence of a long-lived triplet state (Fig. 4D). Concerning the EQEs measurements, these NIR emissive species present a value of 17%, higher than the most common PLQYs of around 10% registered in the region ~750–1000 nm [48].

3.4. Computational studies

To identify the species responsible for the NIR emission, the obtained results were combined with theoretical calculations. Based on previous reports, this type of emission is attributed to polysulfide ($[S_x]^{2-}$) species, such as $[S_2]^{2-}$, $[S_3]^{2-}$, $[S_4]^{2-}$, or $[S_5]^{2-}$ [49–51]. Fig. 5A shows the diffuse reflectance spectra of sample S/Cl = 4.5, superimposed with the simulated absorption spectrum that best fits the experimental results. The simulated absorption spectra were calculated by TD-DFT (Supplementary Table 4) for $[S_3]^-$ (C_{2v}), $[S_2]^{2-}$, $[S_3]^{2-}$ (C_{2v}), $[S_4]^{2-}$ (C_2), $[S_4]^{2-}$ (C_{2h}), and $[S_4]^{2-}$ (C_{3v}), selected due to the small sulfur molecules already reported in these type of aluminosilicate materials. The best fit is obtained with $[S_3]^{2-}$ (with a minimal contribution of $[S_3]^-$) in agreement with the results from EPR spectroscopy, which points to a reduction of the relative amount of paramagnetic species in the sample S/Cl = 4.5, leading us to infer that the dominant species is non-paramagnetic. Fig. 5B displays a schematic representation of the relative energy of the calculated singlet and triplet states of $[S_3]^{2-}$. The respective state symmetries and orbitals are summarized in Supplementary Table 5 and Supplementary Fig. 5.

The experimental transition observed in the diffuse reflectance spectrum, centered at 355 nm (3.49 eV), is in good agreement with the energies calculated for $S_0 \rightarrow S_3$ and $S_0 \rightarrow S_5$ transitions. The intersystem crossing mechanism between $S_1 \rightarrow T_1$, $S_3 \rightarrow T_5$ and $S_5 \rightarrow T_5$ are shown in Supplementary Table 6. In the case of the transitions $S_3 \rightarrow T_5$ and $S_5 \rightarrow T_5$, there are simultaneous spin and orbital changes; thus, the total angular momentum is preserved, allowing the non-radiative transition, while in transition $S_1 \rightarrow T_1$, the conservation of the orbital results in a forbidden transition according to El-Sayed rules [52]. On the other hand, the energy gap (ΔE_{ST}) is much smaller in $S_3 \rightarrow T_5$ and $S_5 \rightarrow T_5$ than in $S_1 \rightarrow T_1$, resulting in a $k_{ISC}^{S_3 \rightarrow T_5}$, $k_{ISC}^{S_5 \rightarrow T_5} \gg k_{ISC}^{S_1 \rightarrow T_1}$. The calculated oscillator strength of S_1 can explain the lack of fluorescence through the natural radiative lifetime. The natural radiative lifetime occurs when there are no nonradiative processes involved. This constant can be calculated through the oscillator strength by equation (4) (where f is the oscillator strength and v_{max} is the frequency of absorption in cm^{-1}) and gives an upper limit to the lifetime of an excited molecule [53].

$$\tau_N = \frac{1.5}{\bar{\upsilon}_{máx}^2 \times f} \quad (4)$$

The $\tau_N^{S_1}$ calculated with the theoretical values in Supplementary Table 5 is about 2.92 × 10^{-6} s, with a corresponding k_N of 3.4 x 10^5 s^{-1}. A typical kinetic constant of internal conversion (k_{IC}) is in order of 10^{12} s^{-1} [[53]]. Therefore, $k_{IC}^{S_1 \rightarrow S_0} \gg k_N^{S_1}$, which explains the lack of fluorescence. Since the singlet states S_3 and S_5 can undergo intersystem crossing to T_5 state, it is expected that $k_{ISC}^{S_3 \rightarrow T_5} + k_{ISC}^{S_5 \rightarrow T_5} \gg k_{IC}$, so that phosphorescence is possible by population of the triplet manifold from higher lying singlet states. The same El-Sayed allowed transition to the triplet manifold can occur by exciting at 266 nm (Supplementary Table 6). By excitation at this wavelength, the performed transient absorption experiment revealed a long living state that can be assigned to $T_1 \rightarrow T_n$ transition (Fig. 4D), which is also in good agreement with the calculated transitions (Supplementary Table 5). Additionally, triplet state T_1 is

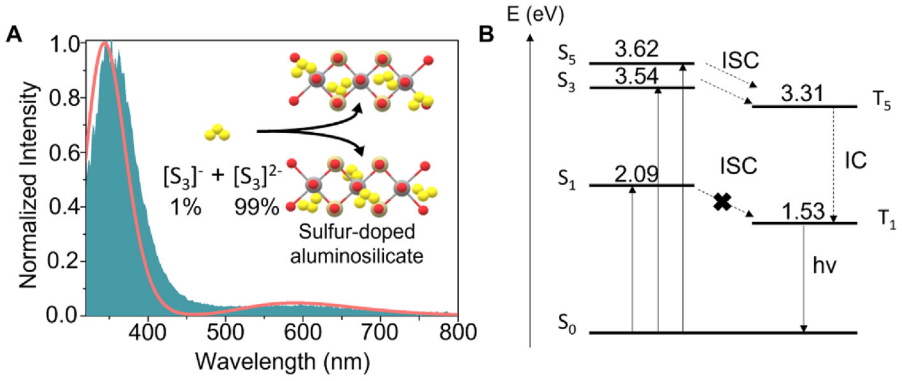

Fig. 5. - Computational studies. (A) Overlap of the Kubelka-Munk spectrum of sample S/Cl = 4.5 (green) and the combined calculated spectra of $[S_3]^{2-}$ and $[S_3]^-$ species (orange). (B) Proposed energy diagram of $[S_3]^{2-}$ clusters.

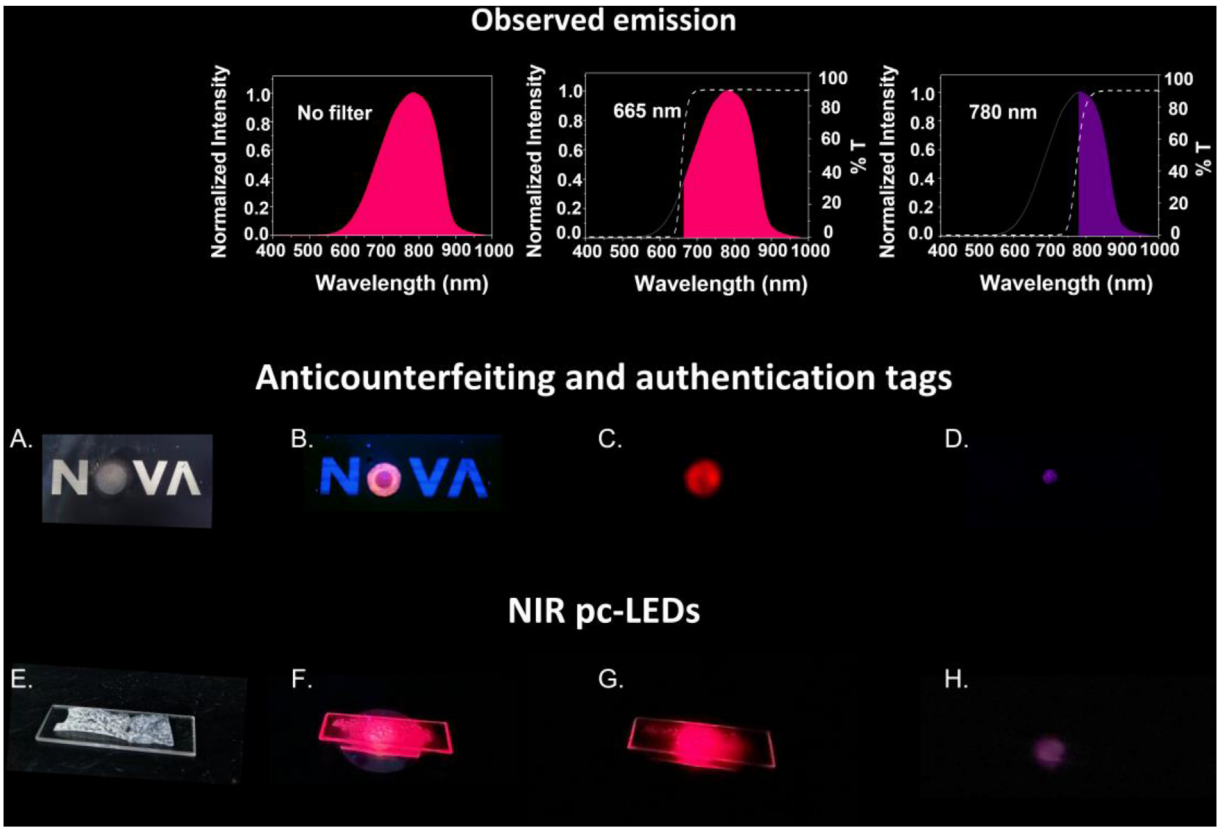

Fig. 6. – Prototypes using sulfur-doped zeolites as authentication and anticounterfeiting tags (Middle) and as NIR phosphor-convert light emitting diodes (Below). Photos were taken by a smartphone under ambient (A, E) and under UV illumination, around λ_{exc} = 365 nm (B–D and F–H). Without any cutoff filter (B, F) and using a 665 nm (C, G) and a 780 nm (D, H) cutoff filters. Note the overlap between the emission spectra of the NIR-emitting sample and the transmission spectra of the cutoff filters used. The filled area under the curve represents the emission detected by the smartphone (Top).

predicted energy at 1.53 eV (809 nm) that matches the long-lived emission values in the NIR region of 1.57 eV (790 nm), see Fig. 4B.

3.5. Suitable applications for these materials

The luminescent properties observed above pointed out the utility of these sulfur-doped zeolites to be used as anticountering and authentication systems and as NIR pc-LEDs (Fig. 6). Here, we demonstrate a proof of concept for both applications. First, two zeonex films, one coated with sample S/Cl = 0.21 (yellow-orange emission) and the other with S/Cl = 4.5 (NIR emission), were deposed in the 'O' of the 'NOVA' logo, printed in an acetate sheet, forming a well-defined pattern (internal 'O' with the NIR emission and the external 'O' with the yellow-orange emission, see Fig. 6B). These coated films are not distinguishable under ambient light (Fig. 6A). In the second experiment, a commercial UV-LED with an excitation wavelength around 365 nm was coated with a zeonex film impregnated with sample S/Cl = 4.5. In both cases, we applied several cutoff filters with different wavelengths in front of the smartphone camera, where up to 780 nm cutoff filter, it was still possible to detect luminescence from the NIR-emitting sample, yet completely invisible with human vision.

4. Conclusions

Nowadays, alternatives to commonly used NIR emitters that lack in availability and stability are required. In this study, we demonstrated that a zeolite-based luminescent material with emission maxima at 790 nm with an EQE of 17% can be simply prepared from sustainable and non-toxic sources. Starting with widely available Na-LTA type zeolite, materials with yellow to NIR emission were prepared by adjusting the sulfur content in the starting materials. Through the analysis of spectroscopy and computational data, we showed that the $[S_2]^-$ species, responsible for the yellow emission of sulfur-doped sodalites at low-sulfur concentrations are replaced by triatomic sulfur clusters $[S_3]^-$ and $[S_3]^{2-}$ when sulfur concentration increases. With our characterization and calculation results, we were able to assign the NIR luminescence to $[S_3]^{2-}$ clusters. This species exhibits an absorption band around 355 nm, displaying a remarkable stokes shift of 1.97 eV. The long emission lifetime and a detected transient absorption confirmed the prepared materials are phosphorescent. Through XRD data, we were also able to demonstrate that the NIR-emitting clusters are present in nepheline and/or carnegieite crystalline phases, which replace sodalite phase at high sulfur concentration. The same luminescence and decay time were also found in samples composed only by nepheline and carnegieite crystalline phases (see Fig. 3 and Supplementary Fig. 4). The optical properties of these materials, with absorption in the UV region and emission mainly in the NIR, with EQE's of about 17% with lifetimes in the millisecond range make them particularly interesting for photonic applications such as anticounterfeiting and authentication tags, light-based communication technologies or as phosphors in the preparation of NIR-LEDs.

Author contribution

C. Viola – Investigation, Formal analysis, Visualization, Writing – Original Draft; C. Laia – Validation, Supervision; M. Outis –

Investigation, Formal analysis; L. Ferreira – Investigation, Formal analysis, Methodology; L. Alves – Investigation, Formal analysis, Methodology; M. Teixeira – Investigation, Formal analysis, Methodology; F. Folgosa – Investigation, Formal analysis, Methodology; J. Lima – Validation, Supervision, Methodology, Writing – Review & Editing; A. Ruivo – Writing – Review & Editing, Formal Analysis, Methodology, Supervision; J. Avó – Writing – Review & Editing, Formal Analysis, Methodology, Supervision.

Declaration of competing interest

The authors declare that they have no known competing financial interests or personal relationships that could have appeared to influence the work reported in this paper.

Data availability

All data supporting the findings of this study are available within the article and the Supplementary Data

Acknowledgment

The authors want to acknowledge the Portuguese Foundation for Science and Technology for funding through the grants SFRH/BD/145009/2019 and SFRH/BPD/120599/2016, the individual contract 2020.00252. CEECIND and several projects PTDC/QUI-QFI/32007/2017, UIDB/04565/2020, UIDP/04565/2020, LA/P/0140/2020, LAQV-REQUIMTE (LA/P/0008/2020, UIDB/50006/2020 and UIDP/50006/2020), VICARTE (UIDP/00729/2020, UIDB/00729/2020) and C2TN (UIDB/04349/2020). MOSTMICRO-ITQB R&D Unit (UIDB/04612/2020, UIDP/04612/2020) and LS4FUTURE Associated Laboratory (LA/P/0087/2020) and by European Union's Horizon 2020 research and innovation program under grant agreement No. 810856.

Appendix A. Supplementary data

Supplementary data to this article can be found online at https://doi.org/10.1016/j.mtchem.2023.101514.

References

[1] T. Shi, C. Huang, Y. Li, F. Huang, S. Yin, Biomaterials 285 (2022), 121535.
[2] M.Y. Berezin, W.J. Akers, K. Guo, G.M. Fischer, E. Daltrozzo, A. Zumbusch, S. Achilefu, Biophys. J. 97 (2009) L22–L24.
[3] P. Jiang, Z. Tian, C. Zhu, Z. Zhang, D. Pang, Chem. Mater. 24 (2012) 3–5.
[4] J.I. Deneff, K.S. Butler, L.E.S. Rohwer, C.J. Pearce, N.R. Valdez, M.A. Rodriguez, T.S. Luk, D.F. Sava Gallis, Angew. Chem., Int. Ed. 60 (2021) 1203–1211.
[5] Z. Zhang, H. Chang, B. Xue, S. Zhang, X. Li, W.K. Wong, K. Li, X. Zhu, Cellulose 25 (2018) 377–389.
[6] A. Zampetti, A. Minotto, F. Cacialli, Adv. Funct. Mater. 29 (2019) 1–22.
[7] J. Cao, L. Wondraczek, Y. Wang, L. Wang, J. Li, S. Xu, M. Peng, ACS Photonics 5 (2018) 4393–4401.
[8] B. Pashaei, S. Karimi, H. Shahroosvand, M. Pilkington, Adv. Funct. Mater. 30 (2020) 1–31.
[9] M. Mao, T. Zhou, H. Zeng, L. Wang, F. Huang, X. Tang, R.J. Xie, J. Mater. Chem. C 8 (2020) 1981–1988.
[10] Z. Jia, C. Yuan, Y. Liu, X. J. Wang, P. Sun, L. Wang, H. Jiang and J. Jiang, Light Sci. Appl., https://doi.org/10.1038/s41377-020-0326-8.
[11] G. Pramanik, J. Humpolickova, J. Valenta, P. Kundu, S. Bals, P. Bour, M. Dracinsky, P. Cigler, Nanoscale 10 (2018) 3792–3798.
[12] E. Alonso, A.M. Sherman, T.J. Wallington, M.P. Everson, F.R. Field, R. Roth, R.E. Kirchain, Environ. Sci. Technol. 46 (2012) 3406–3414.
[13] K.H. Kim, S. Singha, Y.W. Jun, Y.J. Reo, H.R. Kim, H.G. Ryu, S. Bhunia, K.H. Ahn, Chem. Sci. 10 (2019) 9028–9037.
[14] M. Khodadadi Yazdi, P. Zarrintaj, H. Hosseiniamoli, A.H. Mashhadzadeh, M.R. Saeb, J.D. Ramsey, M.R. Ganjali, M. Mozafari, J. Mater. Chem. B 8 (2020) 5992–6012.
[15] A. Khaleque, M.M. Alam, M. Hoque, S. Mondal, J. Bin Haider, B. Xu, M.A.H. Johir, A.K. Karmakar, J.L. Zhou, M.B. Ahmed, M.A. Moni, Environ. Adv. 2 (2020), 100019.
[16] Y. Wada, T. Okubo, M. Ryo, T. Nakazawa, Y. Hasegawa, S. Yanagida, J. Am. Chem. Soc. 122 (2000) 8583–8584.
[17] L. Gigli, R. Arletti, J.G. Vitillo, G. Alberto, G. Martra, A. Devaux, G. Vezzalini, J. Phys. Chem. C 119 (2015) 16156–16165.
[18] M. Lezhnina, F. Laeri, L. Benmouhadi, U. Kynast, Adv. Mater. 18 (2006) 280–283.
[19] H.-T. Sun, M. Fujii, Y. Sakka, Z. Bai, N. Shirahata, L. Zhang, Y. Miwa, H. Gao, Opt. Lett. 35 (2010) 1743.
[20] G.-G. Lindner, K. Witke, H. Schlaich, D. Reinen, Inorganica Chim 252 (1996) 39–45.
[21] A. Ruivo, E. Coutiño-Gonzalez, M. Santos, W. Baekelant, E. Fron, M. Roeffaers, F. Pina, J. Hofkens, C. Laia, J. Phys. Chem. C 122 (2018) 14761–14770.
[22] I. Norrbo, A. Curutchet, A. Kuusisto, J. Mäkelä, P. Laukkanen, P. Paturi, T. Laihinen, J. Sinkkonen, E. Wetterskog, F. Mamedov, T. Le Bahers, M. Lastusaari, Mater. Horiz. 5 (2018) 569–576.
[23] European Commission, Study on the EU's List of Critical Raw Materials, Final Report, Brussels, 2020, 2020.
[24] M. Gaft, G. Panczer, L. Nagli, H. Yeates, Phys. Chem. Miner. 36 (2009) 127–141.
[25] R.D. Kirk, J. Electrochem. Soc. (1954) 461–465.
[26] D. Reinen, G.-G. Lindner, Chem. Soc. Rev. 28 (1999) 75–84.
[27] A. Sidike, A. Sawuti, X. Wang, H. Zhu, S. Kobayashi, I. Kusachi, N. Yamashita, Phys. Chem. Miner. 34 (2007) 477–484.
[28] A. Radulović, V. Dondur, P. Vulić, Z. Miladinović, G. Ćirić-Marjanović, R. Dimitrijević, J. Phys. Chem. Solid. 74 (2013) 1212–1220.
[29] L. Ding, H. Yang, P. Rahimi, O. Omotoso, W. Friesen, C. Fairbridge, Y. Shi, S. Ng, Microporous Mesoporous Mater. 130 (2010) 303–308.
[30] I.F. Chang, J. Electrochem. Soc. 121 (1974) 815–820.
[31] R.Y. Vanagida, A.A. Amaro, K. Seff, J. Phys. Chem. 77 (1973) 805–809.
[32] I.S. Hassan, S.Y.M. Antao, J.O.H.N.B. Parise, Am. Mineral. 89 (2004) 359–364.
[33] B. Hippler, H. Bohm, Z. Kristallogr. 187 (1989) 39–53.
[34] F.W. Barth, E. Posnjak, Z. für Kristallogr. - Cryst. Mater. 81 (1932) 135–141.
[35] R. Dimitrijevic, V. Dondur, P. Vulic, S. Markovic, S. Macura, J. Phys. Chem. Solid. 65 (2004) 1623–1633.
[36] H.G. Hecht, J. Res. Natl. Bur. Stand. 80 (1976) 567–583, 1934.
[37] E. Climent-Pascual, J. Romero De Paz, J. Rodríguez-Carvajal, E. Suard, R. Sáez-Puche, Inorg. Chem. 48 (2009) 6526–6533.
[38] N.V. Chukanov, A.N. Sapozhnikov, R.Y. Shendrik, M.F. Vigasina, R. Steudel, Minerals 10 (2020) 1042.
[39] K. Raulin, N. Gobeltz, V. Hervé, N. Touati, B. Ledé, A. Moissette, Phys. Chem. Chem. Phys. 13 (2011) 9253–9259.
[40] D. Arieli, D.E.W. Vaughan, D. Goldfarb, J. Am. Chem. Soc. 126 (2004) 5776–5788.
[41] B. Ledé, A. Demortier, N. Gobeltz-Hautecœur, J.-P. Lelieur, E. Picquenard, C. Duhayon, J. Raman Spectrosc. 38 (2007) 1461–1468.
[42] R. Kirk, Glass (1955) 22–31.
[43] J.A. Creighton, H.W. Deckman, J.M. Newsam, J. Phys. Chem. 98 (1994) 448–459.
[44] C.L. Angell, J. Phys. Chem. 77 (1973) 222–227.
[45] D.W. Matson, S.K. Sharma, J.A. Philpotts, Am. Mineral. 71 (1986) 694–704.
[46] S. Kowalak, A. Jankowska, S. Zeidler, A.B. Więckowski, J. Solid State Chem. 180 (2007) 1119–1124.
[47] J. Schneider, B. Dischler, A. Räuber, Phys. Status Solidi 13 (1966) 141–157.
[48] A.L. Antaris, H. Chen, S. Diao, Z. Ma, Z. Zhang, S. Zhu, J. Wang, A.X. Lozano, Q. Fan, L. Chew, M. Zhu, K. Cheng, X. Hong, H. Dai, Z. Cheng, Nat. Commun. 8 (2017) 1–11.
[49] F. Blumentritt, C. Latouche, Y. Morizet, Y. Morizet, M.T. Caldes, S. Jobic, E. Fritsch, J. Phys. Chem. Lett. 11 (2020) 4591–4596.
[50] W. Giggenbach, Inorg. Chem. 11 (1972) 1201–1207.
[51] C. Barchasz, Fl Molton, C. Duboc, J.-C. Leprêtre, S. Patoux, F. Alloin, Anal. Chem. 84 (2012) 3973–3980.
[52] C.M. Marian, Wiley Interdiscip. Rev. Comput. Mol. Sci. 2 (2012) 187–203.
[53] K.K. Rohatgi-Mukherjee, Fundamentals of Photochemistry, 1978.
[54] D.T. Petasis, M.P. Hendrich, Quantitative Interpretation of Multifrequency Multimode EPR Spectra of Metal Containing Proteins, Enzymes, and Biomimetic Complexes first ed., vol. 563, Elsevier Inc., 2015.
[55] D.P. Ferreira, D.S. Conceição, F. Fernandes, T. Sousa, R.C. Calhelha, I.C.F.R. Ferreira, P.F. Santos, L.F. Vieira Ferreira, J. Phys. Chem. B 120 (2016) 1212–1220.
[56] L. Vieira Ferreira, I. Ferreira Machado, Curr. Drug Discov. Technol. 4 (2007) 229–245.
[57] D.S. Conceição, L.F. Vieira Ferreira, ChemistrySelect 3 (2018) 773–778.